Hindawi
Shock and Vibration
Volume 2022, Article ID 5257252, 14 pages
https://doi.org/10.1155/2022/5257252

*Research Article*

# High-Speed Penetration Test and Numerical Simulation of Ceramic-Reactive Powder Concrete Composite Target

**Xuezhi Wu,[1] Huihui Zou,[2] Gan Li,[1] Yihao Cheng,[1] and Chunming Song[1]**

[1]*State Key Laboratory of Disaster Prevention & Mitigation of Explosion & Impact, The Army Engineering University of PLA, Nanjing 210007, Jiangsu, China*
[2]*State Key Laboratory of Intense Pulsed Radiation Simulation and Effect, Northwest Institute of Nuclear Technology, Xi'an 710024, China*

Correspondence should be addressed to Chunming Song; ming1979@126.com

Received 22 February 2022; Revised 14 April 2022; Accepted 9 May 2022; Published 22 June 2022

Academic Editor: Junyan Yi



To study the protective performance of ceramic materials against the high-speed penetration of projectiles, seven ceramic-reactive powder concrete (C-RPC) composite targets were designed. Using a 100/30 mm two-stage light-gas gun, penetration tests were performed at 1.4–2.0 km/s. The results showed that the penetration depth of the C-RPC target body first increased and then decreased as the target speed increased, and the corresponding reverse penetration speed was between 1743.2 m/s and 1803.9 m/s. LS-DYNA software was used to perform a wide-speed numerical simulation study of a projectile's high-speed penetration of the composite target, focusing on the analysis of the deformation, mass loss, passivation, and penetration depth of the projectile. Changes in the parameters were compared with the experimental results of a C-RPC penetration test, which together revealed the changes in the damaging effect of the missile's high-speed penetration of the C-RPC composite target. It provided a damage analysis of the high-speed/super-high-speed penetration of the projectile, which provides a reference for targeted protection research.

## 1. Introduction

The rapid development of high-velocity deep-drilling weapons poses a serious threat to protective structures [1–4]. Numerous experimental and theoretical studies [1, 5–7] have shown that traditional concrete materials cannot resist a direct attack from high-velocity, high-caliber weapons. Thus, research into high-strength, high-fracture-resistant protective materials, and their matching composite protective structures has garnered interest in the field of protective engineering. A variety of new materials and composite structures have been intensively studied and applied to protective structures, such as fiber concrete [5], reactive powder concrete (RPC) [6], and corundum-rubble concrete [7]. These materials have improved the anti-penetration ability of protective structures. Ceramic materials possess high strength, high hardness, and low density [8] and have been widely used in armor designs. Many studies have been conducted on the penetration of armored ceramics, including the depth of penetration (DOP) tests, theoretical models, and numerical simulations [8–12]. It has been shown that the use of ceramics in armor materials provides excellent penetration resistance at the current projectile level (<1.8 km/s) and considerable antipenetration protection against future projectile levels (2.5–3 km/s) [8]. Therefore, the application of ceramic materials in protective engineering is expected to further enhance the anti-penetration capability of traditional concrete protective structures. The main role of the ceramic is to blunt and erode the projectile, however, ceramics are brittle. Thus, in composite targets, ceramic tiles are often backed with ductile materials, such as armored steel, aluminum, or fiberglass, to disperse and absorb kinetic energy. Sherman et al. [9] conducted several investigations into the antipenetration performance of alumina ceramics with different thicknesses of steel, aluminum, and fiber-reinforced backplanes. Since most protective engineering structures are concrete-based, ceramic materials must be applied in the form of a composite

with a concrete structure, and their antipenetration performance must be re-evaluated. However, limited research has been performed on the antipenetration performance of ceramic-concrete composite targets. RPC is a concrete material with high strength, high toughness, and low porosity [6]. Experimental studies on RPC targets under projectile impact have been conducted [13, 14], and the results indicated that the antipenetration ability was three times higher than that of ordinary concrete. Some scholars have used experiments and numerical simulations to describe the damage to RPC targets and have modified the penetration depth formula to more accurately predict the projectile parameters during penetration [15, 16]. Therefore, RPC could be composited with ceramics. In terms of the penetration and destructive effects of high-velocity projectiles, extensive research has been carried out on concrete and rock media [4, 17–19], and different low-velocity rigid penetration phenomena have been found in both concrete and rock materials. In this paper, seven ceramic-active powder concrete composite targets (C-RPC targets) were designed, and targets were tested at a velocity range of 1.4–2.0 km/s using a two-stage light gas gun test. The penetration and destruction mechanisms within the C-RPC target were analyzed, which provides a basis for its application in protective engineering.

## 2. Penetration Tests

*2.1. Projectile.* As shown in Figure 1, the ogive nose projectiles used in the penetration tests were machined from 30CrMnSiNi2A steel rods. The length of the projectile was 54 mm, and the diameter was 10.8 mm. The projectile length-to-diameter ratio and caliber radius head (CRH) were 5.0 and 3.0, respectively. The mass of the projectile was 32.45 g. The basic mechanical properties of the material are shown in Table 1.

*2.2. Design of Ceramic-Reactive Powder Concrete Composite Target.* A total of seven C-RPC targets were designed in this experiment. The C-RPC target was composed of a ceramic target and an RPC target, and the composite scheme is shown in Figures 2 and 3. The ceramic target was backed by a cylinder RPC target with a height of 1000 mm and a diameter of 500 mm. To eliminate the influence of the boundary effect, the target plate was surrounded by a 10-mm thick steel pipe. The volume fiber content of RPC is 5%. During on-site construction, it is poured from bottom to top and fully vibrated and stirred to maintain the uniformity of the target to ensure the maximum strength and toughness of the target. Pouring and maintenance are carried out according to Chinese standards and specifications. The ceramic target consisted of nine ceramic blocks with the dimensions of $100 \times 100 \times 20$ mm that were superglued in the shape of a nine-square grid, which was closely combined with the RPC target using a 5 mm thick mortar layer. The gaps between the ceramic target and the steel tube were uniform and were filled with a mortar layer to ensure the integrity of the ceramic target and the RPC target. $Al_2O_3$, $SiO_2$, and CaO


Figure 1: Projectile.

account for 95%, 1.75%, and 3.25%, respectively, in ceramic materials, which are finally processed into finished products through forming process and sintering process, and the mechanical properties of the ceramic were tested according to the relevant national standards of China. The test results are shown in Table 1.

*2.3. Emissions and Measurements.* Experiments were performed using a 100/30 mm two-stage light gas gun that could accelerate a 90 g projectile to 3000 m/s, thus meeting the test requirements. The test system is shown in Figure 4. During the experiment, the first stage of the two-stage light gas gun was driven by high-velocity nitrogen gas, and the second stage was driven by hydrogen gas. The emission velocity was controlled by adjusting the high-pressure gas chamber and the first-stage pump tube air pressure. When the projectile is launched, the air pressure in the secondary pump pipe is between 30 Pa and 50 Pa. After the projectile was accelerated by the two-stage light gas gun, the velocity was measured using the laser light velocity interception method. Then, the shell was separated by a sheller. The velocities were measured to an accuracy of 0.1 m/s. Finally, the target was placed on a target box and then impacted. The trajectory of the projectile was recorded using high-velocity cameras. After the experiment, the macroscopic failure modes of the projectile and target were observed, and the penetration depth, quality, and deformation of the recovered body were measured.

## 3. Results

*3.1. Test Results.* Table 2 shows the main measurements of the penetration tests. A total of seven shots was performed during the penetration test, and the penetration velocity ranged from 1.4 to 2.0 km/s. The table showed that the penetration depth of targets was less than ½ that of the target thickness. Thus, the RPC target in the C-RPC target could be approximated as a semi-infinite target for analysis.

*3.2. Penetration Depth Analysis.* It can be seen from Figure 5 that the penetration depth of C-RPC composite target increased, then decreased, and finally increased again upon increasing the impact velocity. This process can be divided into three stages: ascending stage (<1743.2 m/s), inverse reduction stage (1743.2 m/s << 1803.9 m/s), and stable stage (≥1804 m/s).

Chen [20, 21] et al. derived an expression for the bullet mass loss based on the research of concrete targets with different strengths and combined it with experimental data.

Table 1: Material parameters of ceramic and fiber.

| Material | Density (kg/m$^3$) | Elasticity modulus (GPa) | Strength (MPa) | Hardness | Fracture toughness (MN/m$^{3/2}$) |
|---|---|---|---|---|---|
| 30CrMnSiNi2A | 7850 | 201 | 1352 | HRC50 | — |
| Ceramic | 3650 | 381 | 439 | HRA89 | 4.81 |
| RPC | 2850 | 54 | 176 | — | 11.6 |

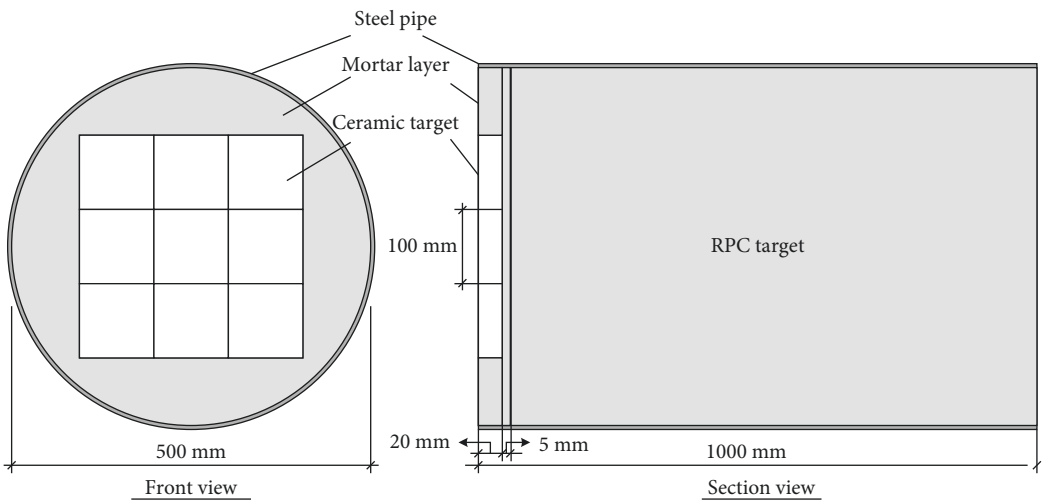


Figure 2: The composition of the C-RPC composite target.

Figure 3: C-RPC composite targets.

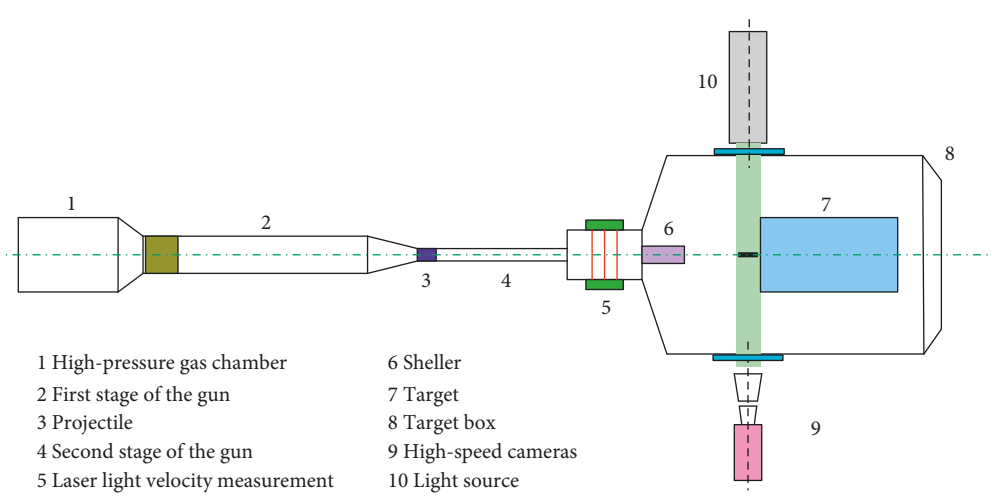


Figure 4: Arrangement diagram of the test.

Table 2: Experimental results.

| No. | Target | Impact velocity (m/s) | Depth of penetration (mm) | Residual mass of projectile (g) | Percentage of residual mass | Remaining projectile length |
|---|---|---|---|---|---|---|
| 1 | C-RPC1 | 1473.9 | 89 | 14.47 | 44.6% | 19.23 |
| 2 | C-RPC2 | 1580.3 | 114 | 12.88 | 39.7% | 19.21 |
| 3 | C-RPC3 | 1743.2 | 139 | 12.62 | 38.9% | 18.17 |
| 4 | C-RPC4 | 1803.9 | 122 | 11.77 | 36.3% | 17.36 |
| 5 | C-RPC5 | 1891.7 | 125 | 11.10 | 34.2% | 16.29 |
| 6 | C-RPC6 | 1958.4 | 125 | —* | —* | —* |
| 7 | C-RPC7 | 1986.0 | 131 | —* | —* | —* |

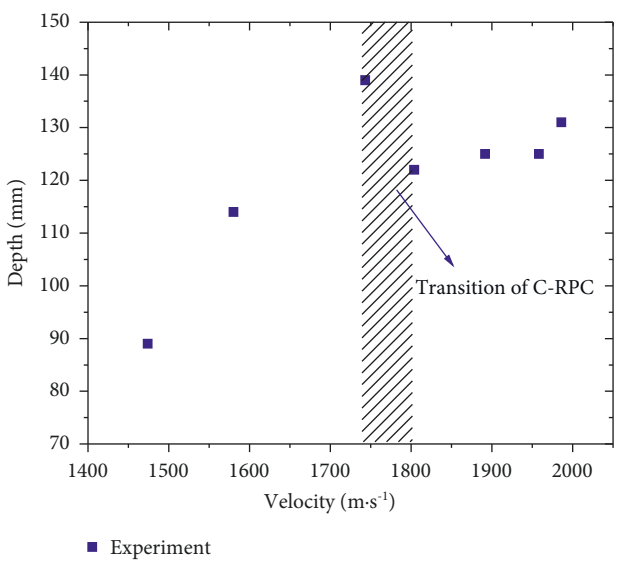


Figure 5: The relationship between the penetration depth and penetration speed.

$$\delta = \frac{\Delta m}{m} = \begin{cases} kI, & I \le 120, \\ C, & I > 120. \end{cases} \tag{1}$$

To obtain the critical penetration speed,

$$v_g = \sqrt{\frac{120 A_t N_1 d_p^3 \sigma_t}{m}}, \tag{2}$$

where $\Delta m$ is the mass loss of the projectile, and $m$ is the mass of the projectile. $A_t$ is the correlation coefficient of projectile penetration, $d_p$ is the diameter of the projectile, $\sigma_t$ is the yield strength of the target, and $N_1$ is the correlation coefficient of the projectile shape.

Calculated according to related literature [20–22], the following values were obtained: $m = 32.45\,g$, $d_p = 1.08$ cm, $N_1 = 1.09$, $\sigma_t = 176\,MPa$, and $A_t = 4.77$. The critical inflection point velocity of the rigid body-semi-fluid of the RPC target body was obtained as $v_g = 1978\,m/s$. Compared with the calculated critical inflection point velocity, the critical velocity (1743.2 m/s) of the missile's high-speed penetration of the C-RPC target occurred much earlier. The projectile first penetrated the ceramic target body during the high-speed impact of the target body. Because of the high strength of the ceramic target body, the passivation and destruction of the projectile head were worse than the penetration of the RPC target body.

According to formula (2) [22], when the projectile velocity $v < 1978\,m/s$, the projectile penetration is still in the rigid body stage during the projectile penetration into a single RPC target, and the abrasion and passivation of the projectile head occur within the test velocity range, indicating that the ceramic target changes the shape of the projectile head. The head of the passivated projectile continues to penetrate the RPC target in the shape of a mushroom head, which is calculated by the Forrestal resistance formula.

$$F = \frac{\pi d^2}{4}\left(S f_c' + N^* \rho_t V^2\right), \tag{3}$$

$d$ is the diameter of the projectile, $\rho_t$ is the target density, $f_c^{'}$ is the unconfined compressive strength of RPC target, $S$ is the target material parameter, $V$ is the projectile velocity during penetration, and $N^*$ is the correlation coefficient of the projectile shape. The density of ceramic target $\rho_t$ and compressive strength $f_c^{'}$ are higher than those of the RPC target, resulting in the impedance of the penetrating ceramic target being much higher than that of the penetrating RPC target, thus reducing the projectile speed.

When the high-speed projectile hits the ceramic target, the contact area between the projectile and the target is in a high-pressure state, and the projectile has plastic flow and a small amount of local damage, resulting in less mass loss and blunting of the projectile head. As the impact velocity exceeds the critical velocity, the damage and mass loss of the projectile increase significantly and sharply, resulting in the rapid decline of its penetration efficiency and the reversal of penetration depth. When the impact velocity continues to

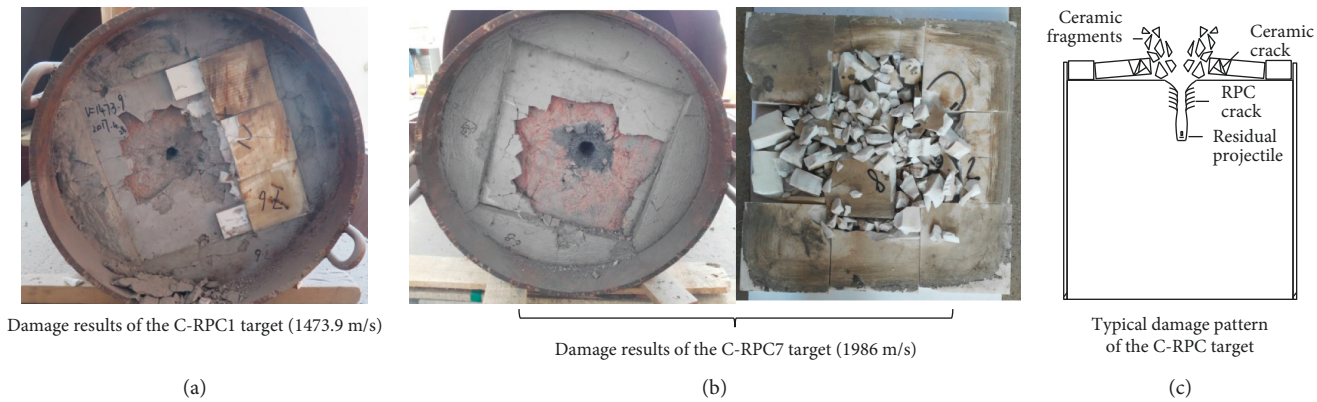


Figure 6: Damage results of C-RPC target. (a) Damage results of the C-RPC1 target. (b) Damage results of the C-RPC7 target. (c) Typical damage pattern of the C-RPC target.

increase and exceeds a certain critical velocity, the projectile will erode and penetrate like a fluid as a whole. The change of penetration mechanism leads to the slow increase of penetration depth with the increase of impact velocity. Therefore, when the projectile penetrates in the wide velocity domain, the penetration depth first increases, then decreases, and then slowly increases with the impact velocity.

*3.3. Target Destruction.* Figure 6(a) shows the failure mode of the C-RPC target after the projectile penetrated it at 1473.9 m/s. The ceramic block with the target body was completely broken, and the adjacent ceramic blocks spalled off from the surface of the RPC target. Since the target of the projectile was not a ceramic block at the center of the ceramic target, the remaining three ceramic blocks did not spall off and were well-preserved. The RPC target formed a ballistic region where the projectile penetrated. The diameter of the ballistic region was approximately three times the diameter of the projectile. A few cracks were generated around the crater, however, no obvious tunnel pit was formed. This result was different from the typical failure mode for a single concrete medium, which was a combination of craters and ballistic tunnels.

As the penetration velocity increased, the degree of damage to the C-RPC composite target worsened. Figure 6(b) shows the failure mode of the projectile after the C-RPC composite target was penetrated at a velocity of 1986.0 m/s. The ceramic target completely spalled off, and the RPC target formed a ballistic tunnel with a diameter of 90 mm, which was approximately 3 to 4 times greater than the diameter of the projectile. The spliced ceramic target morphology is shown in Figure 6(b). The central ceramic block struck by the projectile was completely pulverized, and the four ceramic blocks adjacent to the center position also underwent different degrees of cracking. The basic shape of the ceramic block at the four corners of the target plate remained intact. A typical disruption of the C-RPC target is shown in Figure 6(c).

*3.4. Projectile Damage.* Figure 7 shows the residual shape of the recovered projectile after it penetrated the C-RPC target at 1743.2 m/s. The diameter of the mushroom head was larger. The mass erosion and deformation state of the projectile under high-velocity penetration are closely related to the interaction of the projectile [1, 17, 19]. When the projectile penetrated the C-RPC composite target at a high velocity, the projectile was softened and passivated, firstly, because of the high strength, high hardness, and high-temperature resistance of the ceramic. Then, the ceramic layer was pulverized. When the projectile was inactivated and passivated, the penetration efficiency was greatly reduced. However, the RPC material did not contain coarse aggregates and was highly uniform. Hence, the asymmetric abrasion of the projectile did not readily occur. In the process of penetration, the projectile body erodes from head to tail, the geometric state of the remaining projectile body changes significantly, and the surface color of the projectile body darkens and adheres to a small amount of RPC material, however, the material and mechanical properties of the projectile body do not change.

Figure 7: Residual projectiles after penetrating the C-RPC target at 1743.2 m/s.

## 4. Finite Element Model and Parameters

*4.1. Geometric Model of Projectile and Target.* The LS-DYNA finite element software was used to perform numerical simulations for the high-speed/super-high-speed penetration of the missile into the C-RPC target. TrueGrid preprocessing software was used to establish a two-dimensional symmetrical model of the projectile and the target. The projectile used the node separation method, the nodes at the

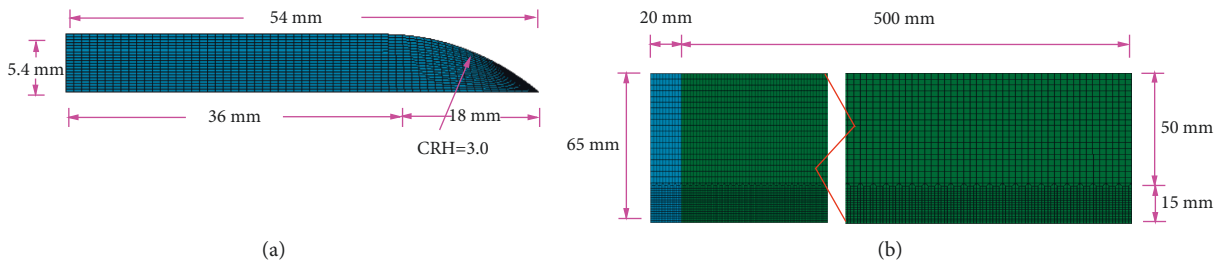


Figure 8: Finite element model. (a) Projectile. (b) Target.

same position used *CONSTRAINED-TIED-NODES-FAILURE for fixed connection constraints, and the elastic nodes reached plastic failure. They opened automatically after a strain of 0.3. The ceramic target body and RPC target body were modeled by the node separation method 15 mm from the centerline. The ceramic target body automatically opened when the plastic strain reached 0.008, and the node automatically opened when the plastic strain of the RPC target body reached 0.015. The other parts were ordinary elements. As shown in Figure 8(a), the material of the projectile was 30CrMnSiNi2A, the length of the oval projectile was 54 mm, the projectile radius was 5.4 mm, the shape coefficient was CRH = 3.0, and the projectile head was 18 mm long. The projectile was divided into 1200 units. As shown in Figure 8(b), the ceramic target adopted a rectangular parallelepiped with a length of 10 mm and a width of 65 mm. The RPC target adopted a rectangular parallelepiped with a length of 500 mm and a width of 65 mm. After the target is impacted by the projectile, the deformation and damage area are significant, which are about 3 times the projectile diameter. The size of this area is 15 mm, and the grid is refined. Beyond this range, the deformation and force of the target are small. Hence, the meshing is large. In the process of simulation, using a refined mesh for all regions will greatly increase the calculation time, however, the improvement of accuracy is insignificant [23]. Therefore, the grid size of the ceramic target body and the RPC target body 15 mm from the centerline was 1 mm × 1 mm, and the grid size of the remaining parts was 2 mm × 2 mm.

*4.2. Material Constitutive Equation.* The calculation adopted the Lagrange algorithm. Since the projectile impacted at a high speed, the impact process involved problems, such as large deformation, high temperature, high pressure, and high strain rate. For the case where the strain rate was less than $10^4\ s^{-1}$, the Johnson-Cook [24] model can be used. This model is suitable for a wide range of strain rates and can simultaneously consider the strain hardening, strain rate hardening, and thermal softening of the material. Hence, it is widely used, and this model requires additional definition of the equation of state. The Johnson-Cook model decouples strain, strain rate, and temperature, and it uses the product relationship to deal with the effects of the three on the dynamic yield stress. The yield stress is expressed as follows:

$$\sigma_y = \left(A + B\bar{\varepsilon}_p^n\right)\left(1 + Cln\dot{\varepsilon}^*\right)\left(1 - T_H^m\right), \tag{4}$$

$A$—reference strain rate and initial yield stress at reference temperature. $B$, $n$—material strain hardening modulus and hardening index. $C$, $m$—material strain rate strengthening parameters and thermal softening index. $\bar{\varepsilon}_P$—effective plastic strain. $T_H$—relative temperature. $\dot{\varepsilon}^*$—effective plastic strain rate.

According to formula (4), the yield strength $\sigma_y$ of the material is mainly related to the initial yield strength A, strain strengthening, strain rate, and temperature, which can be obtained through static load and other related tests. The basic mechanical parameters $A$, $B$, $n$, and $C$ of 30CrMnSiNi2A were obtained through a series of quasistatic uniaxial tensile experiments and dynamic Hopkinson compression bar experiments at a strain rate of $10^{-3}$. The specific values are shown in Table 1.

The Johnson-Cook model uses the maximum failure plastic strain $\varepsilon f$ to decide whether to delete an element.

$$\varepsilon f = \left[D_1 + D_2 \exp D_3\sigma^*\right]\left[1 + D_4 \ln \varepsilon^*\right]\left[1 + D_5 T^*\right], \tag{5}$$

where $\sigma^*$ is the ratio of the pressure to effective stress. $D_i$ is stored as an extra history variable in shell elements. The $D_i$ value is determined by the failure coefficient values of 30CrMnSiNi2A with different hardness in reference [25].

The EOS_GRUNEISEN state equation was used to describe the pressure state of the projectile when it hit the target. The accuracy was high for the high-speed impact of the flyer, and the expression was as follows:

$$P = \frac{\rho_0 C^2 u\left[1 + (1 - \gamma_0/2)u - a/2u^2\right]}{\left[1 - (S_1 - 1)u - S_2u^2/u + 1 - S_3u^3/(u+1)^2\right]^2} + (\gamma_0 + au)E. \tag{6}$$

$C$ is the intercept of the $u_s$–$u_p$ curve, $s_1$, $s_2$, and $s_3$ are the slope coefficients of the $u_s$–$u_p$ curve, $\gamma_0$ is the GRUNEISEN coefficient, and its expression is as follows:

$$\gamma_0 = \frac{\alpha c^2}{C_V} \times \frac{1}{(1 + \alpha\gamma_0 T)}. \tag{7}$$

In the formula, $\alpha$ is the thermal expansion coefficient of the body, $c$ is the hydrodynamic sound velocity, $C_V$ is the constant volume specific heat, and $T$ is the temperature. Under normal conditions, the $\gamma_0$ value of the same substance is the same.

$a$ is the first-order volume correction, which is a dimensionless quantity, $u = \rho/\rho_0 - 1$, and $E$ is the internal energy

Table 3: Basic parameters of the projectile.

| RO (g· cm$^{-3}$) | $A$ (MPa) | $B$ (MPa) | $N$ | $C$ | EPSO (S) | CP (J/(kg•°C)) |
|---|---|---|---|---|---|---|
| 7.8 | 1352 | 1042 | 0.52 | 0.036 | 0.001 | 477 |
| $D_1$ | $D_2$ | $D_3$ | $D_4$ | | | |
| 0.154 | 4.2 | 5.5 | 0.007 | | | |
| EOS_GRUNEISEN | | C (m·s$^{-1}$) | $S_1$ | $\gamma_0$ | a | |
| | | 4522 | 1.49 | 2.17 | 0.46 | |

of the material. The parameters in the equation of state are obtained from reference [26]. The main parameters are shown in Table 3.

For RPC materials, the HOLMQUIST-JOHNSON-CONCRETE [27] model was used. The HJC model considers how the strain rate, hydrostatic pressure, and damage accumulation affect the strength. The damage model considers the effects of large strain, high strain rate, and high pressure. In the HJC model, the specific expression of the normalized equivalent intensity of the intensity model is as follows:

$$\begin{aligned} \sigma^* &= \left[A(1-D) + BP^{*N}\right]\left[1 + C\ \ln\left(\dot{\varepsilon}^*\right)\right], \\ \sigma^* &= \frac{\sigma}{f_c'}, \\ P^* &= \frac{P}{f_c'}, \\ \dot{\varepsilon}^* &= \frac{\dot{\varepsilon}}{\dot{\varepsilon}_0}, \\ T^* &= \frac{T}{f_c'}, \end{aligned} \tag{8}$$

where $\sigma^*$ is the dimensionless equivalent stress, $\sigma^* \leq$Smax, Smax is the maximum normalized dimensionless strength limit. $\sigma$ is the actual equivalent stress, $f_c'$ is the static uniaxial compressive strength, P is the pressure, $\dot{\varepsilon}_0 = 1.0\text{s}^{-1}$ is the reference strain rate, and T is the tensile strength. $D$ is the damage parameter, $P^*$ is the normalized pressure, and $\dot{\varepsilon}^*$ is the dimensionless strain rate. $A$ is the normalized cohesive strength, $B$ is the normalized pressure hardening, $N$ is the pressure-hardening exponent, and $C$ is the strain rate coefficient.

$D$ is a function of plastic volumetric strain, equivalent volumetric strain, and pressure $P$, and its expression is as follows:

$$D = \sum \frac{\left(\Delta\varepsilon_p + \Delta u_p\right)}{D_1\left(P^* + T^*\right)^{D_2}}. \tag{9}$$

$\Delta\varepsilon_p$ and $\Delta u_p$ represent the equivalent plastic strain increments and plastic volumetric strain increments in a cyclic integral calculation. $D_1$ and $D_2$ are material damage constants, and $D_1(P^* + T^*)^{D_2} \geq \varepsilon_{\min}^f$.

The state equation of the HJC model is divided into three parts. The first part is the linear elastic segment. When $P \leq \text{P}_{\text{crush}}$, the material is in an elastic state. The bulk modulus of elasticity $K = P_{\text{crush}}/u_{\text{crush}}$, where $P_{\text{crush}}$ and $u_{\text{crush}}$ represent the crushing critical pressure and critical bulk strain in the uniaxial compression test, respectively. In the elastic region, the state equation of loading and unloading is as follows:

$$P = \frac{K}{u}. \tag{10}$$

The second part is the crushing section. When $P_{\text{crush}} < P < P_{\text{lock}}$, the material is in a plastic state. In this interval, with the increase of pressure and plastic volumetric strain, the air is pressed out, the holes are compressed and completely closed, the pores inside the concrete gradually become smaller, and the material becomes a dense medium.

$$\begin{aligned} P &= P\text{crush} + K\text{crush}\,(u - u\text{crush}), \\ K\text{crush} &= \frac{P_{\text{lock}} - P_{\text{crush}}}{u_{\text{lock}} - u_{\text{crush}}}. \end{aligned} \tag{11}$$

The third part is the compaction section. When $P \geq P_{\text{crush}}$, the material is in a high-pressure state, and the material is regarded as a continuous dense medium. At this time, the relationship between pressure and volume is as follows:

$$P = K_1\overline{u} + K_2\overline{u}^2 + K_3\overline{u}^3. \tag{12}$$

In the formula, $\overline{u} = (u - u_{\text{lock}})/(1 + u_{\text{lock}})$, $u_{\text{lock}} = \rho/\rho_0 - 1$, and K1, K2, K3 are constants, which are obtained by experimental fitting. The materials in reference [28] are the same as those in this paper, and the relevant parameters of the RPC material are obtained from reference [28] on the basis of the test. The main parameters of the model are shown in Table 4.

The ceramic material adopted the JOHNSON-HOLMQUIST-CERAMICS [29]model (JH2 model for short). The JH2 model was used to describe the change law of the brittle material strength with damage, pressure, strain rate, etc., and it considered the damage evolution process. It is widely used in ceramic simulations.

The JH2 model couples the strength of the brittle material under any damage with the strength of the brittle material when it is not damaged, the strength of the brittle material when it is completely damaged, and the damage value of the brittle material, and the expression is as follows:

$$\sigma^* = \sigma_i^* - D\left(\sigma_i^* - \sigma_f^*\right). \tag{13}$$

In the formula, $\sigma_i^*$ is the dimensionless equivalent strength of the material in a completely undamaged state, $\sigma_f^*$ is the dimensionless equivalent strength of the material in a completely damaged state, and $D$ is the damage parameter of the material.

Table 4: RPC model parameters.

| $\rho_0$ (kg·m$^{-3}$) | $G$ (GPa) | $Fc$ (MPa) | $T$ (MPa) | $C$ | $A$ | $B$ | $N$ | $S_{\max}$ | EPSO (s) | $\varepsilon^f_{\min}$ | $D_1$ | $D_2$ | $P_C$ (MPa) | $U_C$ | $P_L$ (MPa) | UL | $K_1$ (GPa) | $K_2$ (GPa) | $K_3$ (GPa) |
|---|---|---|---|---|---|---|---|---|---|---|---|---|---|---|---|---|---|---|---|
| 2850 | 14.86 | 176 | 5.0 | 0.007 | 0.79 | 1.6 | 0.61 | 12.5 | 1.0 | 0.01 | 0.04 | 1.0 | 19 | 0.001 | 850 | 0.1 | 85 | −171 | 208 |

Table 5: Main parameters of the ceramic model.

| $\rho_0$ (kg·m$^{-3}$) | $G$ (GPa) | $A$ (GPa) | $B$ (GPa) | $C$ | $M$ | $N$ | $S_{\max}$ (GPa) | $T$ (GPa) | $D_1$ | $D_2$ | $K_1$ (GPa) | $K_2$ (GPa) | $K_3$ (GPa) |
|---|---|---|---|---|---|---|---|---|---|---|---|---|---|
| 3650 | 109.7 | 88 | 43.9 | 0.007 | 0.6 | 0.64 | 1 | 0.262 | 0.005 | 0.83 | 229 | 191.4 | 111.5 |

The dimensionless equivalent strength of the material in a completely undamaged state is expressed as follows:

$$\sigma_i^* = A\left(P^* + T^*\right)^N \left(1 + C \ln \dot{\varepsilon}^*\right). \tag{14}$$

In the formula, $P^* = P/P_{HEL}$, $T^* = T/P_{HEL}$, and $\dot{\varepsilon}^* = \dot{\varepsilon}/\dot{\varepsilon}_0$.

The dimensionless equivalent strength of the material in the fully damaged state can be expressed as follows:

$$\begin{aligned} \sigma_f^* &= B\left(P^*\right)^M \left(1 + C \ln \dot{\varepsilon}^*\right), \\ \sigma_f^* &\le \sigma_{f\,\max}^*. \end{aligned} \tag{15}$$

In the formula, $A$, $B$, $C$, $M$, and $N$ are the fitting parameters of the material, $P$ is the hydrostatic pressure, $T$ is the maximum hydrostatic tensile strength, $P_{HEL}$ is the hydrostatic compressive strength of the material under the elastic limit of Hugoniot, $\dot{\varepsilon}$ is the dynamic load, $\dot{\varepsilon}_0$ represents the reference strain rate, $P^*$ represents the equivalent hydrostatic pressure of the dimensionless material, $T^*$ represents the maximum equivalent hydrostatic tension of the dimensionless material; $\dot{\varepsilon}^*$ represents the material equivalent strain rate of the dimensionless; $\sigma_{f\,\max}^*$ is the maximum equivalent crushing strength of the nondimensionalized material, i.e., the $S_{\max}$ value in Table 3.

The material damage parameter $D$ can be expressed as follows:

$$D = \sum \frac{\Delta\varepsilon_p}{D_1\left(P^* + T^*\right)^{D_2}}. \tag{16}$$

In the formula, $D_1$ and $D_2$ are the material damage coefficients. $\Delta\varepsilon_p$ represents the cumulative integral of the effective plastic strain of the material in one cycle.

The material state equation is as follows:

$$P = K_1\mu + K_2\mu^2 + K_3\mu^3. \tag{17}$$

In the formula, P is the hydrostatic pressure of the material, and $K_1$ is the bulk modulus of the material. $K_2$ and $K_3$ are the parameters of the equation of state obtained by experimental fitting, and $\mu$ is the specific volume of the material, which is related to the material density.

$$\mu = \frac{\rho}{\rho_0} - 1, \tag{18}$$

where $\rho_0$ is the original density of the material, and $\rho$ is the instantaneous density of the material under a certain hydrostatic pressure. The ceramic parameters here are obtained from reference [26]. The main parameters are shown in Table 5.

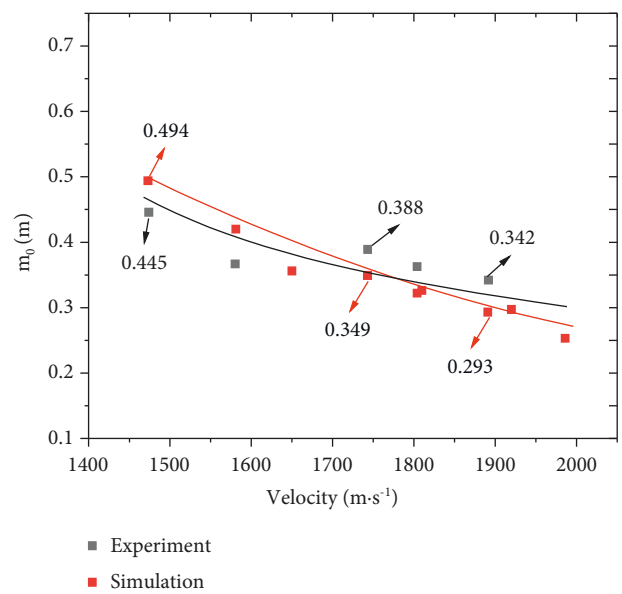


Figure 9: Mass loss of the projectile vs. velocity.

*4.3. Numerical Simulation Verification.* Figure 9 shows that the simulated value and experimental value of the projectile mass under different penetration speeds were basically the same. Both show a linear downward trend, and the error of the mass ratio was within 5%, demonstrating the accuracy of the numerical simulation. The mass loss of the projectile gradually decreased upon increasing the impact velocity, and there was no major inflection point. It also proved that the mass loss did not occur because of the velocity reversal phenomenon caused by the penetration of the C-RPC target. Figure 10 is a comparison diagram of the simulated value of the penetration depth of the projectile and the experimental value. The simulated speed of the projectile was the upper critical inflection point at 1743 m/s, which is in good agreement with the experimental value. The lower critical inflection point velocity was 1810 m/s, which is consistent with the experimental value of 1804 m/s. Because of the influence of the nonuniformity of the target, the penetration depth fluctuates with the increase of the projectile impact velocity. In the simulation process, the mean square error (MSE) of penetration depth is 4.95%, which demonstrates the accuracy of the numerical simulation.

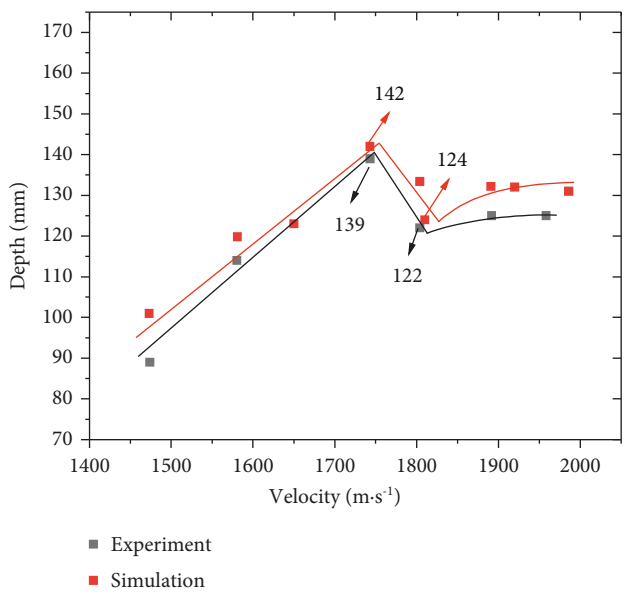


Figure 10: Penetration depth vs. velocity.

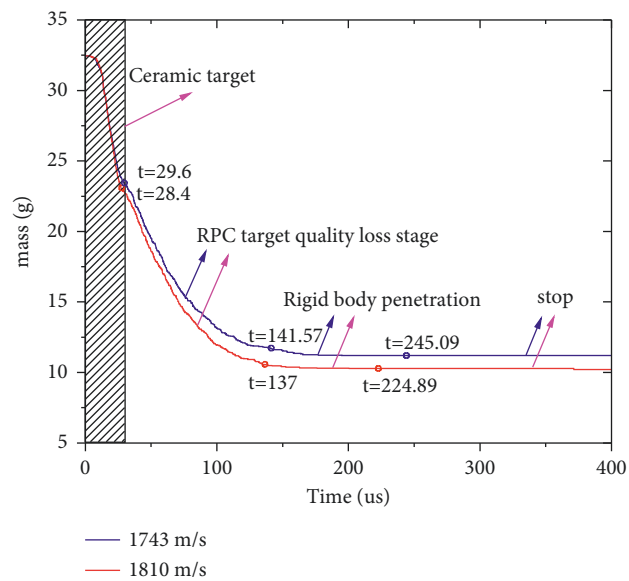


Figure 11: Time-course diagram of missile mass loss.

During the simulation process, when the impact velocity of the projectile is less than 1743.2 m/s, as the projectile head hits the ceramic target, the unit strain of the projectile head becomes greater than the failure plastic strain of the projectile, resulting in the unit being squeezed and separating the projectile. The penetration depth increases gradually with the increase of the impact speed. When the critical speed is exceeded, the mass loss of the projectile increases and the degree of passivation of the projectile head increases, and the plastic region of the projectile moves upward. As the projectile exceeds 1803.9 m/s, the projectile enters the pseudofluid penetration stage, the projectile suffers severe mass loss, the plastic region further extends to the projectile tail, and the penetration depth increases with the increase of the impact speed. The finite element model can better reflect the variation law of projectile penetration depth.

*4.4. Projectile Mass Change Trends.* Figure 11 is a time-history chart of the mass loss of the projectile at impact velocities of 1743 m/s and 1810 m/s. The change law of the projectile mass was basically the same when the projectile penetrated the C-RPC target. This process involved two stages. In the first stage, the mass of the projectile declined. At this stage, the mass of the projectile basically decreased in a quadratic form, and the greater the impact speed, the higher the mass-loss rate of the projectile. During the penetration of the ceramic target body, the mass loss rate was significantly higher than the loss rate after entering the RPC target body. When the time was $t = 28.4\,\mu s$ and $t = 29.6\,\mu s$, the mass loss in the ceramic target body, respectively, accounted for 27.80% and 29.24% of the total mass loss of the projectile. After entering the RPC target, the mass loss continued to increase, and the loss rate slowed down. At $t = 137\,\mu s$ and $t = 141.57\,\mu s$, the mass loss in the RPC target at the two impact speeds accounted for 37.3% and 38.16% of the original mass of the bullet. Because the structure of the projectile changed during the penetration of the ceramic target, the mass loss in the RPC target was very similar to the semifluid-fluid penetration of the projectile into rock, concrete, and other targets. The difference is that 1743 m/s is the upper critical inflection point of the penetration depth reduction. At the same time, a large mass loss occurred at the upper critical inflection point during the penetration of ordinary rocks [17]. At this point, the concrete target was still in the rigid body stage, and the mass loss was very small. The existence of the ceramic target changed the penetration mechanism of the projectile, which made the projectile enter the semifluid-fluid stage earlier.

In the second stage, when the speed of the projectile body during penetration was lower than a certain critical value, the projectile body mass remained basically unchanged and continued to penetrate the RPC target body. At this time, the projectile body was regarded as a rigid body, and the projectile body reached the penetration limit. Afterwards, there was a short rebound phase because of the elastic recovery of the material, after which the projectile stopped moving. From the above analysis, it can be seen that at the initial stage of projectile penetration, the energy of the projectile was greatly reduced by mass reduction. During the penetration of the ceramic target, the impact of the ceramic target on the quality of the projectile was significant.

*4.5. Change Law of Projectile Body.* During the penetration of the C-RPC target, the morphological change in the ceramic target is an important aspect. Here, changes in the projectile were compared at impact velocities of 1743 m/s and 1810 m/s. The time was $10\,\mu s$, $20\,\mu s$, and $30\,\mu s$. It can be seen from Figure 12 that at a certain impact speed, the head deformation of the projectile increased over time, while the damage patterns of the projectile under the two impact speeds at the same time were basically the same.

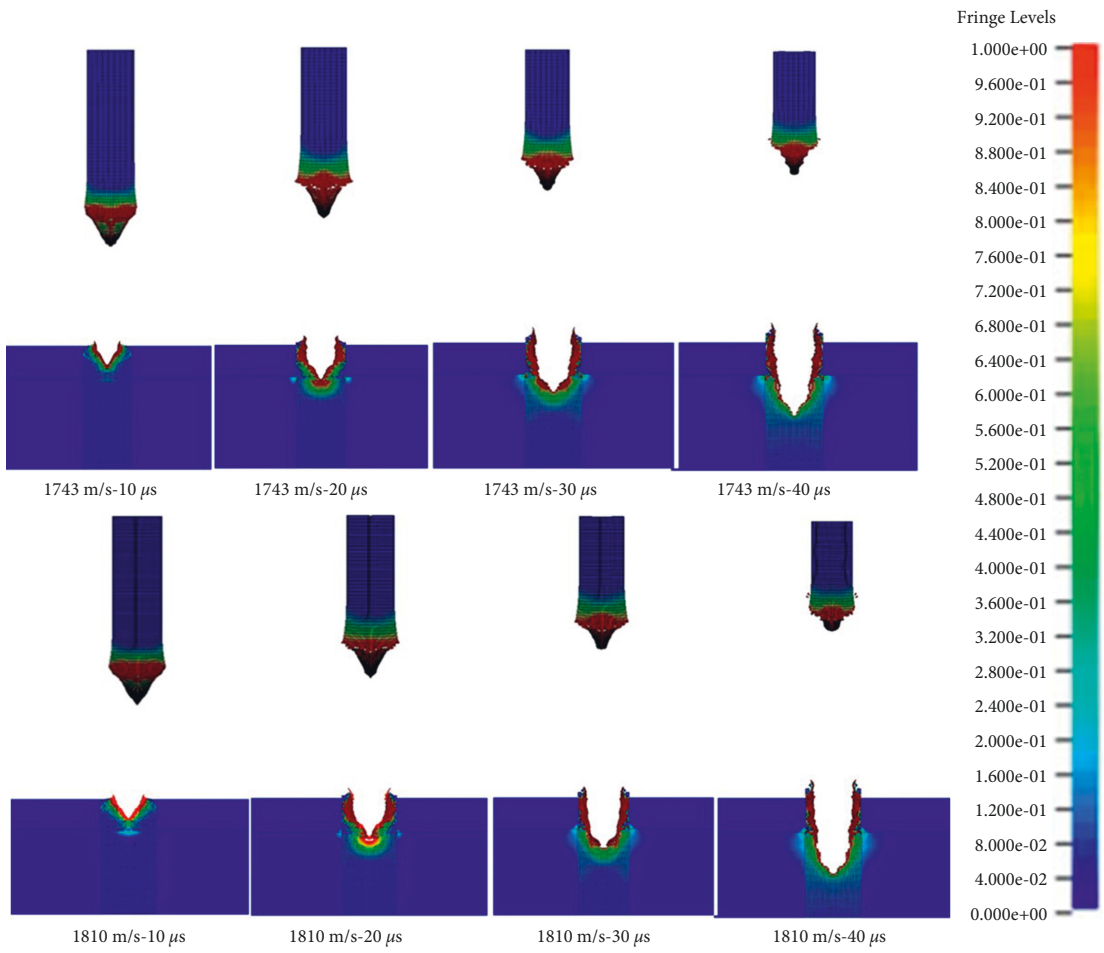


Figure 12: Changes in the shape of the projectile.

At 10 $\mu$s, the head of the projectile had just entered the ceramic target body, the head deformed, cracks formed at the joint between the projectile and the projectile, and some elements of the projectile were broken and peeled. The compression deformation of the projectile at 1810 m/s was significantly higher than at 1743 m/s. The greater the impact speed, the sharper the projectile, and the greater the deformation. The warhead broke and deformed seriously at 20 $\mu$s. The fragments of the projectile were stripped off, and the broken plane of the projectile was blunt and thick. The projectile diameter became wider, and the projectile length became shorter than the original projectile. The target unit fractured, and the ceramic target body fragments spattered to the outside, which also demonstrated the accuracy of the schematic diagram of the typical damage morphology of the C-RPC target in Figure 6(c). At 30 $\mu$s, the projectile body continued its destruction at 20 $\mu$s. The broken warhead continued to penetrate the target body under the push of the projectile body. Compared with the original projectile body, the projectile length at this time changed greatly.

The plastic strain value of the projectile was between 0.3 and 0.35. In Figure 12, the effective plastic strain in the red and green areas exceeded the plastic strain of the projectile. Hence, the projectile presented fluid characteristics. It is an important reason for the deformation and quality loss of the projectile. The ceramic target played a major role in changing the structure, reducing the mass, and dissipating the energy of the projectile. The projectile entered the RPC target body at 40 $\mu$s, and combined with the experiment in this article, it can be seen that the RPC target did not show a large crater effect. In fact, from existing test data [30], the pure RPC target showed no obvious pit-forming effect. The composite target had a high resistance and low pit-forming tendency. These features can be applied to protect against high-speed/super-high-speed weapons that destroy surfaces.

Figure 13 shows changes in the length and diameter of the fracture surface of the projectile during the penetration of the ceramic target. Overall, the projectile diameter increased over time. The change in the projectile diameter at an impact velocity of 1810 m/s at 10 $\mu$s was slightly higher than that at 1743 m/s. The higher the impact velocity, the greater the change in the projectile diameter, however, a greater impact velocity was obtained at 20 $\mu$s. The projectile diameter decreased when the velocity was high because the head of the projectile broke, and some units peeled off the projectile over time. The damage to the projectile increased with time, which led to this experimental phenomenon.

The maximum projectile diameter at the same impact velocity appeared at 20 $\mu$s, and the drop at 30 $\mu$s was also caused by the unit peeling off because of damage to the

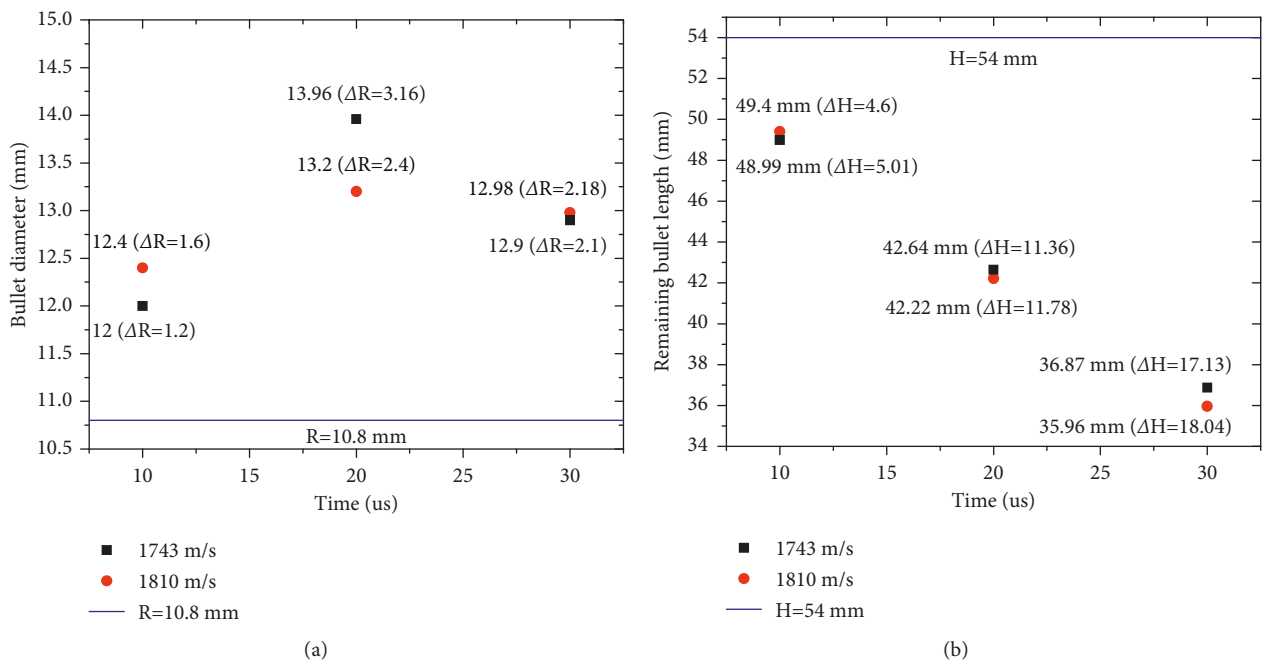


Figure 13: Change in the projectile diameter and projectile length over time. (a) Projectile diameter. (b) Projectile length.

projectile body. The change in the maximum projectile diameter in the figure was 3.16 mm and 2.4 mm, respectively, accounting for 29.26% and 22.22% of the original projectile diameter. The ceramic target had a significant influence on the projectile diameter, where the length of the projectile decreased linearly over time. The head of the projectile just penetrated the ceramic target at 30 $\mu$s. The projectile diameter and length of the projectile at the three time points reflected changes in the projectile during the penetration of the ceramic target. The projectile length data show that the impact of the ceramic target body on the projectile body gradually accumulated over time. At 10 $\mu$s and 20 $\mu$s, the head of the projectile body had just invaded the target body. The deformation of the head was mainly plastic, and the cumulative deformation was small. Hence, the change in the length of the projectile was basically the same. After 20 $\mu$s, the head of the projectile broke, and the force of the projectile was related to the broken warhead at the front. The impact of the projectile diameter after passivation gradually increased. There were two impact speeds at 30 $\mu$s. The projectile length (0.91 mm) began to change, and the percent difference under the two impact speeds at 30 $\mu$s was 31.722% and 33.41%, respectively.

From the perspective of the degree of change in projectile diameter, the ceramic target body affected the projectile. The impact of the structure was obvious. The high-strength ceramic target body destroyed the shape and structure of the bullet, and the bullet body had a shape similar to a flat bullet at the bottom of the ceramic target body. Before entering the RPC target, the change in the projectile's diameter and body at the impact velocity of 1810 m/s was higher than that at 1743 m/s. It is one of the factors that led to the depth reversal of the projectile after it entered the RPC target.

*4.6. The Law of Velocity and Acceleration of the Projectile.* Figure 14 shows the acceleration curves at impact velocities of 1743 m/s and 1810 m/s. The acceleration of the projectile fluctuated greatly at each impact velocity. The projectile was subjected to the combined action of tensile and compressive stress waves during the high-speed penetration of the target. Because of the uneven force on the surface of the projectile, the stress wave was also uneven. The projectile was superimposed by the loading and unloading waves, causing the acceleration to fluctuate.

The acceleration of the projectile when it initially entered the ceramic target body increased rapidly, and the maximum value appeared during penetration. The peak times at the speeds of 1743 m/s and 1810 m/s were 8.4 $\mu$s and 9.3 $\mu$s, respectively, and the peak values were 18.45 ($-10^6$ m/s), 19.65 ($-10^6$ m/s), which increased upon increasing the speed. Because the ceramic target material has the characteristics of high hardness and high strength, the projectile bears high resistance in the process of impacting the ceramic target. Hence, the acceleration curve rises suddenly. The duration of this process is between 8 $\mu$s and 10 $\mu$s at this time, and the projectile penetrates about half of the thickness of the ceramic target. Because the ceramic target is made of brittle material, the remaining ceramics near the missile appear to be broken, which leads to the reduction of resistance and acceleration in the process of further penetration. As the projectile penetrates the ceramic target and enters the RPC target, the force on the projectile is relatively uniform. Hence, the acceleration begins to enter the stable stage. According to Newton's second law, the resistance of the projectile during the penetration of the ceramic target was much greater than that of the RPC target. Considering the overall strength and to provide suitable protection, the thickness of the ceramic target body can be reduced to make

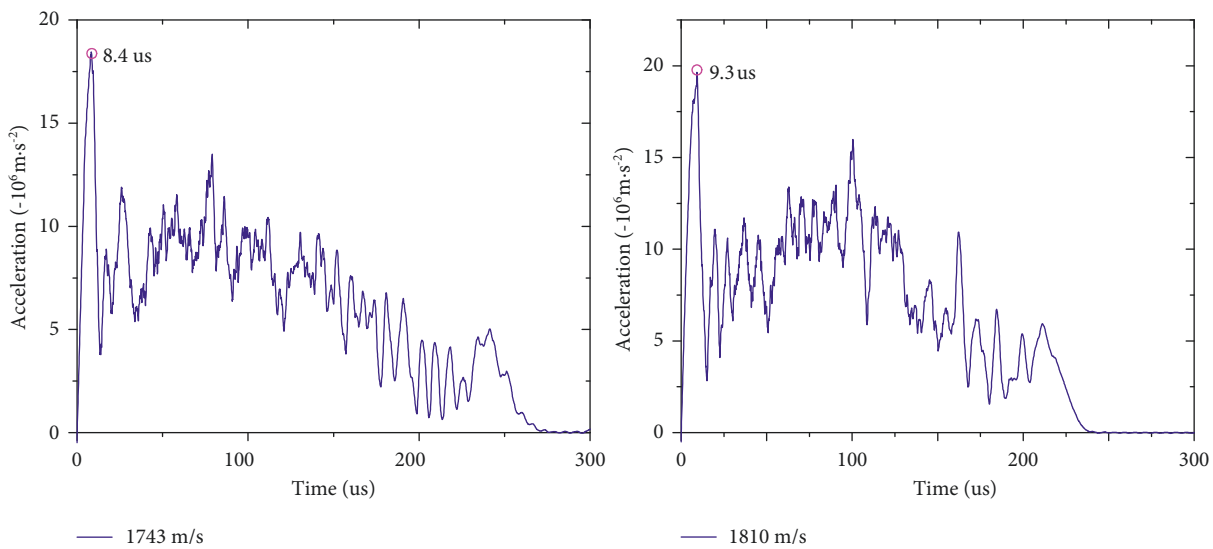


Figure 14: Acceleration curves.

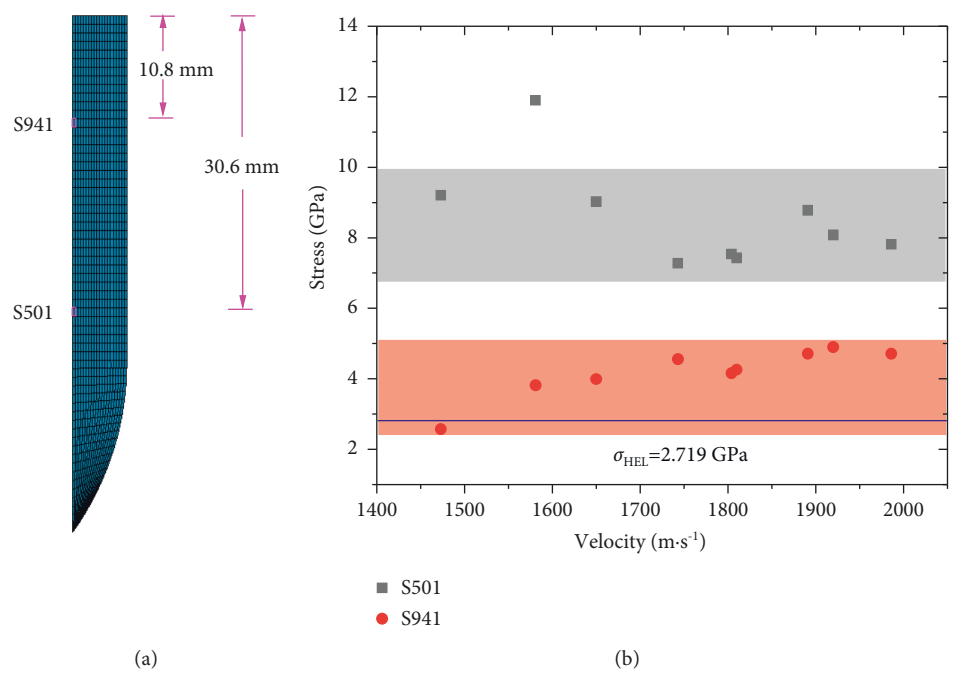


Figure 15: Selected element and maximum stress value. (a) Unit location. (b) Stress.

the protective structure lighter and more economical. The acceleration curve of the projectile reflects the variation law of the hindered resistance in the process of projectile penetration, and it fully shows the antipenetration performance of the target.

*4.7. The Law of Projectile Stress Change.* While the projectile hit the C-RPC target at a high speed, the projectile bore greater impact stress. As shown in Figure 15(a), the maximum output stress of the two units at 10.8 mm and 30.6 mm from the bullet's centerline was selected for comparison. When the element stress exceeded the Hugoniot elastic limit (HEL), the element entered the plastic phase, and the bullet's Hugoniot elastic limit was $\sigma_{HEL}$ = 2.719 GPa. From the point of view of the maximum stress of the two elements, the closer to the warhead, the greater the maximum stress. As the velocity increased, the two elements gradually approached their maximum stress.

As shown in Figure 15(b), the S501 unit was abraded by the target because of its proximity to the warhead within the simulation speed range. The maximum stress exceeded $\sigma_{HEL}$, and the unit entered the plastic stage. When the impact velocity was 1581 m/s, the maximum stress was relatively high. In addition to the calculation error, the stress of the

projectile was affected by the combined action of the tensile wave and compression wave during penetration, however, it was less affected by the transmission wave of the unit near the warhead. The force was uneven during the penetration process, and the stress appeared uneven during superposition, which led to this phenomenon.

After the velocity exceeded 1743 m/s, the maximum stress decreased. Because the projectile experienced a pressure increase during penetration, the greater the velocity, the faster the abrasion speed of the projectile. Thus, the maximum stress did not increase after the impact velocity exceeded 1743 m/s. When pressed to the corresponding level, part of the projectile unit was destroyed. Hence, the maximum stress decreased.

The S941 unit was close to the tail of the projectile, and there was no abrasion within the simulated range. The maximum stress exceeded the value of $\sigma_{HEL}$, except for the impact velocity of 1473 m/s, and the maximum stress increased. The length and speed of the target body gradually decreased, and the force of the projectile gradually decreased upon decreasing the speed of the projectile. When the force of the projectile decreased below the failure stress, the unit in the plastic stage was unloaded to the elastic stage, and the projectile was in the rigid body state and penetrated the target body until it stopped. The unit that reached or exceeded $\sigma_{HEL}$ penetrated the target body with its original shape after being unloaded, and the original plastic deformation was retained, which is one of the factors that resulted in the formation of the mushroom head shape.

The appearance of a large plastic zone in the bullet indicates that the projectile experienced semifluid and fluid penetration during the early stage of penetration. The penetration mechanism of the projectile in the simulation was different from that of a rigid body and more similar to a semifluid or fluid penetration mechanism.

## 5. Design of a Protective Structure

Ceramic protective materials have excellent anti-high-speed penetration performance, and their combination with an RPC can further improve this. However, when designing a combination of ceramic materials and concrete materials, attention should be paid to the speed range of the projectile to prevent material waste. From the destruction morphology of ceramic materials (Figure 6), it can be seen that ceramic materials were very brittle, making it necessary to strengthen constraints when compounding with concrete materials to give full play to the high strength and high hardness of ceramic materials. In addition, during the research and practice of protective structures, a variety of shielding materials with good antipenetration performance have been proposed [1], however, their antipenetration effects are all based on test data obtained from the low-speed penetration stage, which is not applicable to the design of protective structures against high-speed penetration. Therefore, the high-speed penetration resistance of the new ballistic material needs to be re-evaluated.

## 6. Conclusion

In this paper, penetration tests and numerical simulations of a ceramic-RPC composite target within the range of 1.4–2.0 km/s were carried out. By analyzing the macroscopic damage shape and penetration depth of the projectile/target, the conclusions obtained are as follows:

(1) The penetration depth of the C-RPC target showed a three-stage trend of first increasing, then decreasing, and then slowly increasing upon increasing the penetration speed, however, there was no rigid penetration stage. In this experiment, the C-RPC composite target exhibited a penetration reversal of the projectile, and the corresponding reversal speed was between 1743.2 and 1803.9 m/s.

(2) According to numerical simulations, there was a mass decline stage and rigid body penetration stage during projectile penetration into the C-RPC target, and the ceramic target had a significant impact on the mass loss of the projectile. When the projectile penetrated the ceramic target body, fracture occurred, and the projectile body was reduced and its diameter increased. The ceramic target body had a significant impact on the structure of the projectile.

(3) The maximum stresses of the two elements measured in the projectile basically exceed the Hugoniot elastic limit. The closer to the projectile, the greater the stress. As the impact velocity increased, the maximum stress difference at different positions of the projectile gradually decreased, while the plastic zone was enlarged, and the projectile exhibited semifluid/fluid penetration properties.

(4) There were obvious fluctuations in the acceleration of the projectile, however, the overall trend was a decline. As the impact velocity increased, the maximum acceleration of the projectile gradually increased, and changes in the structure of the projectile by the ceramic target also affected the projectile's penetration of the RPC target.

(5) The conclusions of the antipenetration performance of this new shielding material in the low-speed penetration stage need to be re-evaluated before it can be used in high-speed penetration protective structures.

## Data Availability

The data used to support the findings of this study are available from the corresponding author upon request.

## Conflicts of Interest

The authors declare that there are no conflicts of interest regarding the publication of this paper.

## Acknowledgments

The authors would like to acknowledge the financial support from the National Natural Science Funds of China (Grant

nos. 11772355and 12002358), the Natural Science Foundation of Jiangsu Province, China (Grant no. BK20190570), the China Postdoctoral Science Foundation, (Grant no. 2018M643853), and Frontier Innovation Project of Army Engineering University of PLA (grant no. KYFYJQZL2005) for conducting experiments.

## References

[1] H. Q. Ren, C. M. Mu, and C. R. Liu, *Penetration Effect of Precision Guided Weapons and Engineering protection*, The Science Press, Beijing, 2016.

[2] A. J. Piekutowski, M. J. Forrestal, K. L. Poormon, and T. L. Warren, "Penetration of 6061-T6511 aluminum targets by ogive-nose steel projectiles with striking velocities between 0.5 and 3,0 km/s," *International Journal of Impact Engineering*, vol. 23, no. 1, pp. 723–734, 1999.

[3] Z. Rosenberg, E. Marmor, and M. Mayseless, "On the hydrodynamic theory of long-rod penetration," *International Journal of Impact Engineering*, vol. 10, no. 1–4, pp. 483–486, 1990.

[4] J. Li, M. Wang, Y. Cheng, and Y. Qiu, "Analytical model of hypervelocity penetration into rock," *International Journal of Impact Engineering*, vol. 122, pp. 384–394, 2018.

[5] J. Feng, W. W. Sun, Z. L. Liu, C. Cui, and X. Wang, "An armour-piercing projectile penetration in a double-layered target of ultra-high-performance fiber reinforced concrete and armour steel: experimental and numerical analyses," *Materials & Design*, vol. 102, pp. 131–141, 2016.

[6] C. Y. Ni, R. Hou, H. Y. Xia et al., "Perforation resistance of corrugated metallic sandwich plates filled with reactive powder concrete: experiment and simulation," *Composite Structures*, vol. 127, pp. 426–435, 2015.

[7] Y. L. Xue, D. G. Tang, W. X. Chen, Z. Z. Li, D. P. Li, and M. L. Yao, "Experimental and analytical study on the penetration of corundum-rubble concrete subjected to projectile impact," *Shock and Vibration*, vol. 2017, Article ID 1396567, 10 pages, 2017.

[8] V. Hohler, A. J. Stilp, and K. Weber, "Hypervelocity penetration of tungsten sinter-alloy rods into aluminum," *International Journal of Impact Engineering*, vol. 17, no. 1–3, pp. 409–418, 1995.

[9] D. Sherman, "Impact failure mechanisms in alumina tiles on finite thickness support and the effect of confinement," *International Journal of Impact Engineering*, vol. 24, no. 3, pp. 313–328, 2000.

[10] R. R. Franzen, D. L. Orphal, and C. Anderson, "The influence of experimental design on depth-of-penetration (DOP) test results and derived ballistic efficiencies," *International Journal of Impact Engineering*, vol. 19, no. 8, pp. 727–737, 1997.

[11] D. Sherman and T. Ben-Shushan, "Quasi-static impact damage in confined ceramic tiles," *International Journal of Impact Engineering*, vol. 21, no. 4, pp. 245–265, 1998.

[12] R. Zaera, S. Sánchez-Sáez, J. L. Pérez-Castellanos, and C. Navarro, "Modelling of the adhesive layer in mixed ceramic/metal armours subjected to impact," *Composites Part A: Applied Science and Manufacturing*, vol. 31, no. 8, pp. 823–833, 2000.

[13] T. Ge, Y. Pan, and K. Tan, "Study on resistance of reactive powder concrete to impact," *Chinese Journal of Rock Mechanics and Engineering*, vol. 26, no. 1, pp. 3 554–563 557, 2007.

[14] D. R. Wang, T. Ge, Z. P. Zhou, and M. Y. Wang, "Investigation of calculation method for anti-penetra tion of reactive powder steel fiber conc rete (RPC)," *Explosion and Shock Waves*, vol. 26, no. 4, pp. 367–372, 2006.

[15] S. Xu, F. Zhou, Q. Li et al., "Comparative study on performance of UHTCC and RPC thick panels under hard projectile impact loading," *Cement and Concrete Composites*, vol. 122, Article ID 104134, 2021.

[16] S. Xu, P. Wu, F. Zhou, Q. Li, and B. Chen, "Experimental investigation and numerical prediction on resistance of reactive powder concrete to multiple penetration," *Explosion and Shock Waves*, vol. 41, no. 6, pp. 68–83, 2021.

[17] G. Li, C. M. Song, Y. Y. Qiu, and M. Y. Wang, "Theoretical and experimental studies on the phenomenon of penetration depth reverse reduction in the penetration of granite by hyper-velocity projectiles," *Chinese Journal of Rock Mechanics and Engineering*, vol. 37, pp. 60–66, 2017.

[18] A. Dawson, S. Bless, S. Levinson, B. Pedersen, and S. Satapathy, "Hypervelocity penetration of concrete," *International Journal of Impact Engineering*, vol. 35, no. 12, pp. 1484–1489, 2008.

[19] X. W. Chen and Q. M. Li, "Transition from nondeformable projectile penetration to semihydrodynamic penetration," *Journal of Engineering Mechanics*, vol. 130, no. 1, pp. 123–127, 2004.

[20] X. W. Chen, L. L. He, and S. D. Yang, "Modeling on mass abrasion of kinetic energy penetrator," *European Journal of Mechanics - A: Solids*, vol. 29, no. 1, pp. 7–17, 2010.

[21] X. W. Chen and Q. M. Li, "Deep penetration of a non-deformable projectile with different geometrical characteristics," *International Journal of Impact Engineering*, vol. 27, no. 6, pp. 619–637, 2002.

[22] M. J. Forrestal, B. S. Altman, J. D. Cargile, and S. Hanchak, "An empirical equation for penetration depth of ogive-nose projectiles into concrete targets," *International Journal of Impact Engineering*, vol. 15, no. 4, pp. 395–405, 1994.

[23] J. A. Zukas, *Introduction to Hydrocodes*, Elsevier Science, Amsterdam, Netherlands, 2004.

[24] G. R. Johnson and W. H. Cook, "A constitutive model and data for metals subjected to large strains, high strains rates and high temperatures," in *Proceedings of the 7th International Symposition on Ballistics*, vol. 21, pp. 541–547, The Hague, Netherlands, April 1983.

[25] L. I. lei, X. Zhang, X. Wu, F. Gao, and C. Liu, "Dynamic constitutive and damage parameters of 30CrMnSiNi2A teel with different hardnesses," *Chinese Journal of High Pressure Physics*, vol. 31, no. 3, pp. 239–248, 2017.

[26] H. Zou, C. Song, M. Wang, and D. Wang, "Experimental and numerical simulation study on spherical projectiles impacting ceramic targets at high speed," *Protective Engineering*, vol. 40, no. 4, pp. 16–23, 2018.

[27] T. J. Holmquist and G. R. Johnson, "A computational constitutive model for glass subjected to large strains, high strain rates and high pressures," *Journal of Applied Mechanics*, vol. 78, no. 5, 2011.

[28] W. Yin, C. Song, Y. Cheng, C. Chu, F. Gao, and D. Wen, "Numerical simulation for the anti-penetration property of $Al_2O_3$ ceramics-RPC composite targe," *Protective Engineering*, no. 5, pp. 37–42, 2015.

[29] T. J. Holmquist, D. W. Templeton, and K. D. Bishnoi, "Constitutive modeling of aluminum nitride for large strain, high-strain rate, and high-pressure applications,Constitutive modelling of aluminum nitride for large strains,high strain rates, and high pressures applicatons," *International Journal of Impact Engineering*, vol. 25, no. 3, pp. 211–231, 2001.

[30] H. Zou, C. Song, D. Wang, and D. Wen, "Anti-penetration tests for ceramic-reactive powder concrete composite targets," *Journal of Vibration and Shock*, vol. 38, no. 11, pp. 146–151, 2019.